Supplementary Information

# Restriction of Intramolecular Bending (RIB) Enables the Quantitative Design of AIEgens

Weijie Chi,[1,2#] Jianfeng Dai,[3#] Chengxu Yan,[3] Davin Tan,[1] Zhiqian Guo,[3,*] Xiaogang Liu[1,*]

[1]Fluorescence Research Group, Science, Math and Technology Cluster, Singapore University of Technology and Design, 8 Somapah Road, 487372 Singapore, Singapore

[2]Department of Chemistry, School of Science, Hainan University, Haikou 570228, China

[3]Key Laboratory for Advanced Materials and Joint International Research Laboratory of Precision Chemistry and Molecular Engineering, Shanghai Key Laboratory of Functional Materials Chemistry, Frontiers Science Center for Materiobiology and Dynamic Chemistry, Institute of Fine Chemicals, School of Chemistry and Molecular Engineering, East China University of Science & Technology, Shanghai 200237, China

[#]These authors contributed equally

* xiaogang_liu@sutd.edu.sg; guozq@ecust.edu.cn

# Computational Methods

The density functional theory (DFT) and time-dependent DFT (TD-DFT) calculations were conducted using *Gaussian 16*.[1] All structure optimizations in the ground and excited states were performed without constraints using M06-2X functional[2] and the TZVP basis.[3] Solvation effects (in chloroform or ethanol) were taken into account using the SMD solvent model.[4] Frequency calculations were performed to confirm that we obtained stable structures without imaginary vibrational frequencies.

In ONIOM calculations, a central molecule was treated as a high layer and was calculated with the quantum mechanics (QM) method at the M06-2X/TZVP level, while the surrounding molecules were treated as a low layer and were simulated using the molecular mechanics (MM) method. For the MM part, the universal force field (UFF) was employed. Atomic charges were calculated using Multiwfn code[5] to fit the electrostatic potential using the ChelpG method at the M06-2X/TZVP level.

Docking studies were carried out to explore the binding mode of bovine serum albumin and dye **13** using AUTODOCK tools.[6] Before docking, polar-H atoms were added to the bovine serum albumin followed by Gasteiger charges calculation using AUTODOCK tools. Default settings were used for all other parameters of docking. PyMol package[7] was used to visualize the binding interactions between dye **13** and bovine serum albumin.

Based on the perturbation theory and Fermi's golden rule, the rate constant for non-radiation decay can be written as

$$k_{nr} = \frac{|V_{10}|^2}{\hbar^2} \sqrt{\frac{\pi}{a}} \, exp\left( -\frac{\left(E_{10} - \frac{\lambda}{\hbar}\right)^2}{4a} \right) \qquad (1)$$

$$a = \sum_k \left(n_k + \frac{1}{2}\right) S_k \omega_k^2 \qquad (2)$$

where $\lambda$ is the reorganization energy, $n_k$, $\omega_k$, and $S_k$ are the mean number of phonons, vibrational frequencies, and HR factor of model k. $S_k$ is given by

$$S_k = \frac{\omega_k}{2\hbar} D_k^2 \qquad (3)$$

in which $D_k$ is the displacement difference between the most stable structures of ground and excited states of vibrational mode *k*.

The three equations 1-3 showed that the larger HR factor and reorganization energy would lead to a significant rate constant for non-radiation decay. In our work, the Molecular Materials Property Prediction Package 1.0 (MOMAP 1.0) was used to analyze various vibration modes and their contributions to Huang-Rhys (HR) factors and reorganization energy.[8]

# Computational Results

To verify the reliability of the computational method, we compared the calculated geometrical parameters of **1** with its experimental X-ray crystallography data.[9] The relevant results were shown in Table S1. We showed that the calculated bond lengths and key dihedral angles are in good agreement with the experiment data, indicating that the selected computational method is appropriate.

Table S1. Geometrical parameters of **1** as derived from X-ray crystallography and computational studies.
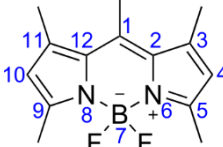
| | Parameters | Experimental (XRD) | Calculated (DFT) |
|---|---|---|---|
| Bond lengths (Å) | C1-C2 | 1.398 | 1.398 |
| | C2-C3 | 1.426 | 1.426 |
| | C3-C4 | 1.379 | 1.382 |
| | C4-C5 | 1.386 | 1.402 |
| | C5-N6 | 1.342 | 1.335 |
| | N6-B7 | 1.534 | 1.552 |
| | B7-N8 | 1.528 | 1.553 |
| | N8-C9 | 1.335 | 1.333 |
| | C9-C10 | 1.396 | 1.407 |
| | C10-C11 | 1.373 | 1.384 |
| | C11-C12 | 1.416 | 1.426 |
| | C12-C1 | 1.393 | 1.397 |
| | C2-N6 | 1.402 | 1.394 |
| | C12-N8 | 1.402 | 1.392 |
| Dihedral angles (°) | ∠C11C12C1C2 | 180 | 176.6 |
| | ∠N7B6N5C4 | 180 | 177.7 |

Table S2. Calculated dihedral angle ($\theta$, °) of **1**–**12** in the ground and excited states in chloroform.

| Molecules | Ground state | Excited state |
|---|---|---|
| **1** | 173 | 168 |
| **2** | 165 | 156 |
| **3** | 172 | 158 |
| **4** | 178 | 176 |
| **5** | 178 | 175 |
| **6** | 177 | 174 |
| **7** | 178 | 176 |
| **8** | 179 | 178 |
| **9** | 180 | 180 |
| **10** | 179 | 173 |
| **11** | 180 | 180 |
| **12** | 172 | 145 |

Table S3. Calculated total reorganization energy and contributions from low-frequency vibrations.

| Molecules | Reorganization energy ($cm^{-1}$) | Contributions due to low-frequency vibrations (%) |
|---|---|---|
| **1** | 483 | 25 |
| **2** | 1156 | 49 |
| **3** | 3147 | 45 |
| **4** | 337 | 10 |
| **5** | 353 | 15 |
| **6** | 403 | 10 |
| **7** | 316 | 8 |
| **8** | 296 | 12 |
| **9** | 349 | 0 |
| **10** | 460 | 23 |
| **11** | 324 | 0 |
| **12** | 7131 | 57 |
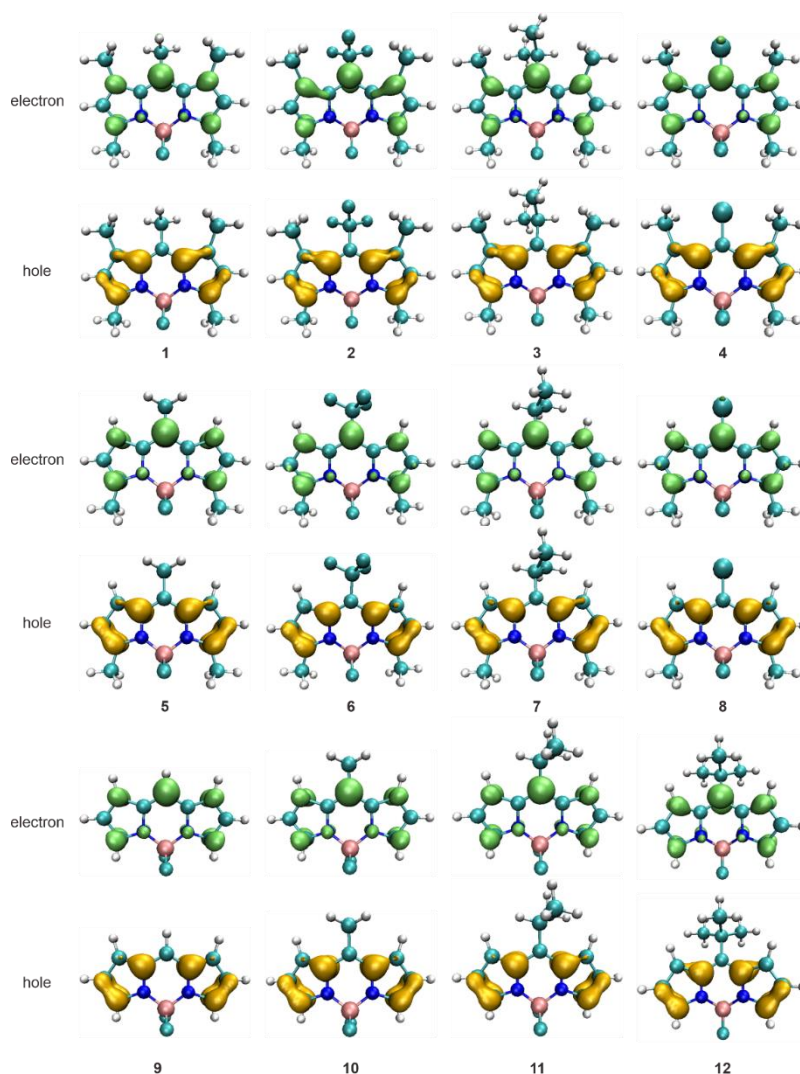
Figure S1. The distributions of electrons and holes of twelve BODIPY dyes in the excited state at M06-2X/TZVP level.
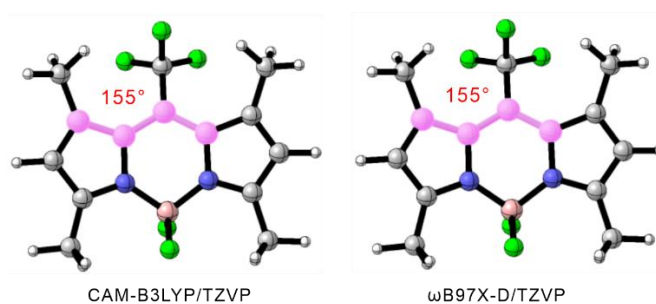


Figure S2. Optimized structures of compound 2 in the excited state using the CAM-B3LYP and ω-B97XD functionals with the TZVP basis set in chloroform.
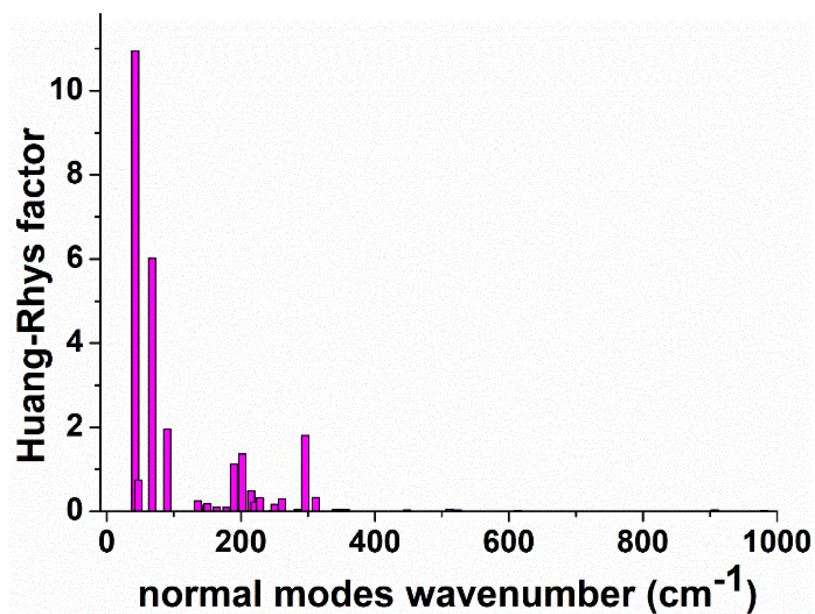
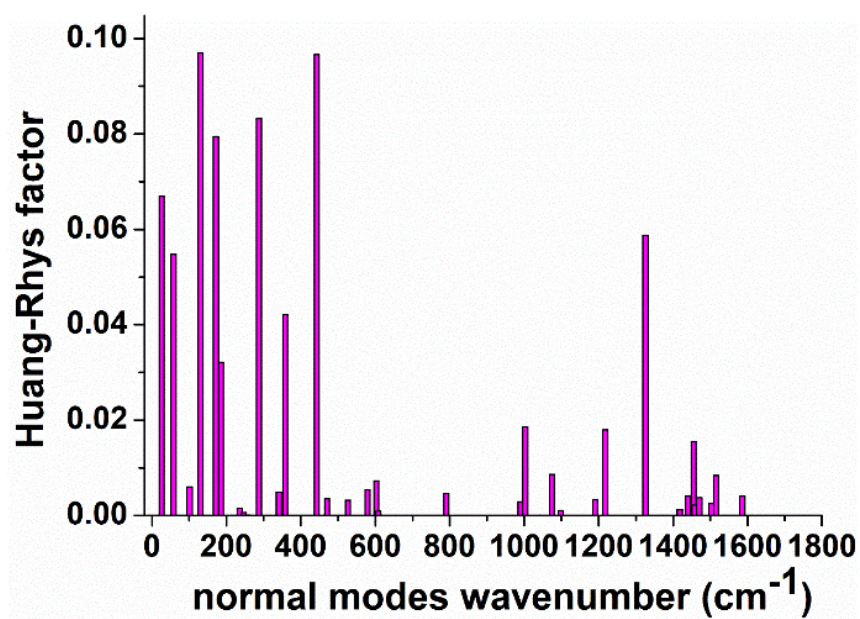Figure S3. Calculated Huang-Rhys factors versus the normal mode wavenumber for **3.**



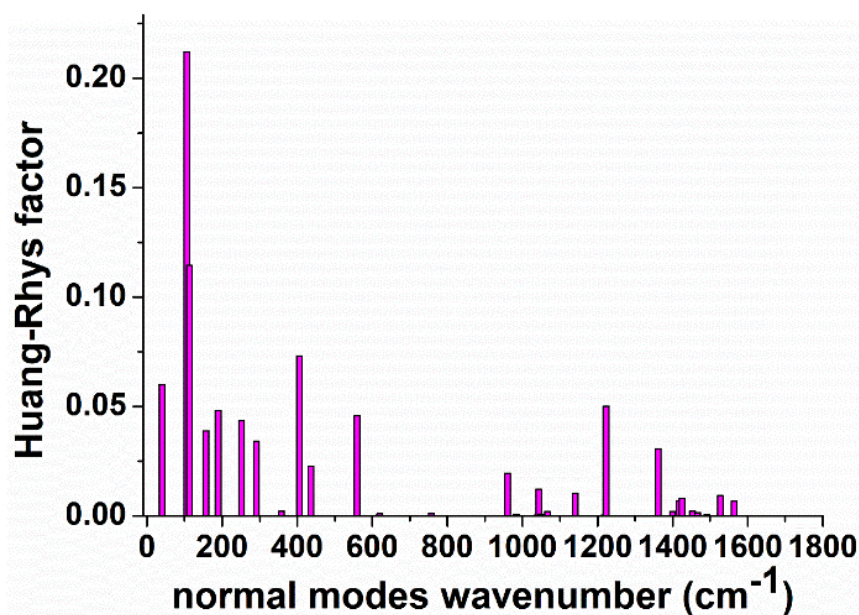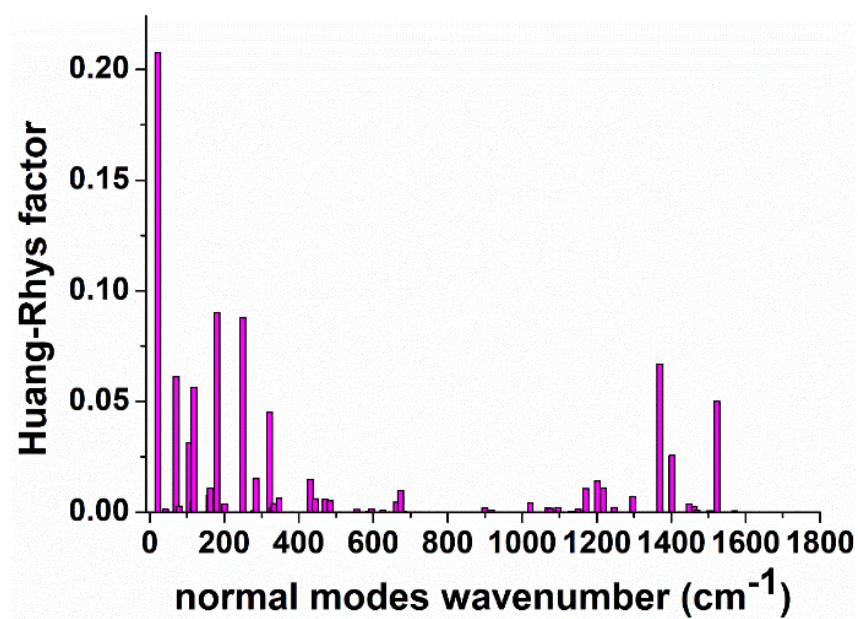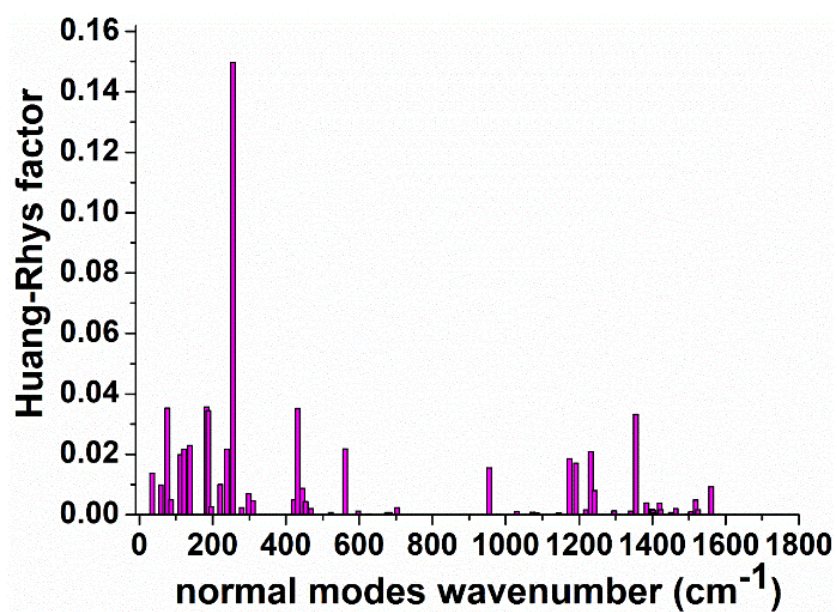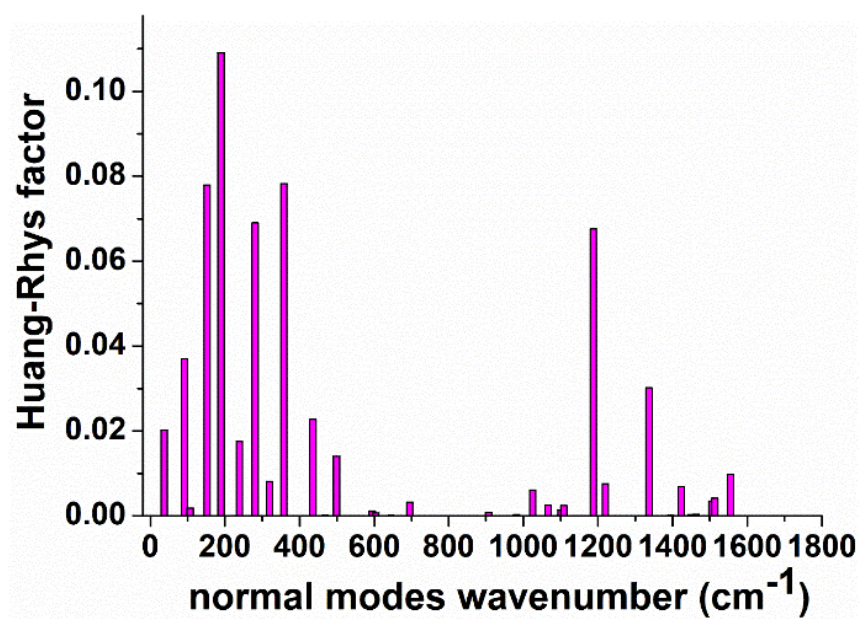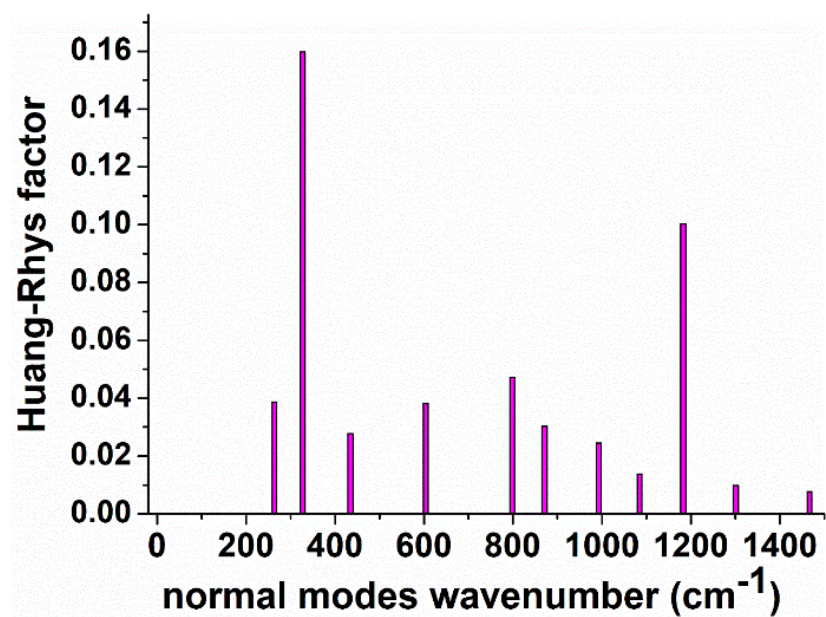Figure S4. Calculated Huang-Rhys factors versus the normal mode wavenumber for **4.**

Figure S5. Calculated Huang-Rhys factors versus the normal mode wavenumber for **5**.



Figure S6. Calculated Huang-Rhys factors versus the normal mode wavenumber for **6**.
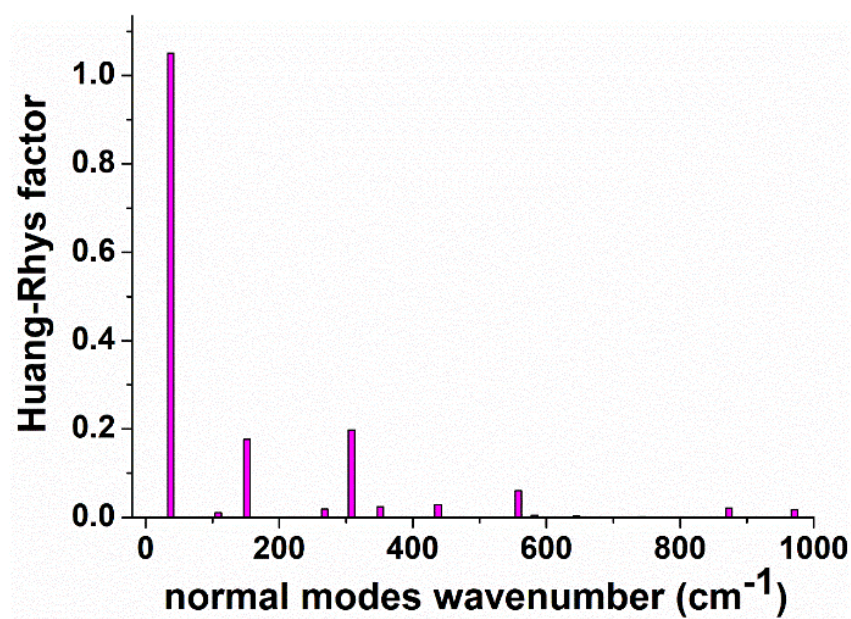
Figure S7. Calculated Huang-Rhys factors versus the normal mode wavenumber for **7**.



Figure S8. Calculated Huang-Rhys factors versus the normal mode wavenumber for **8**.

Figure S9. Calculated Huang-Rhys factors versus the normal mode wavenumber for **9**.



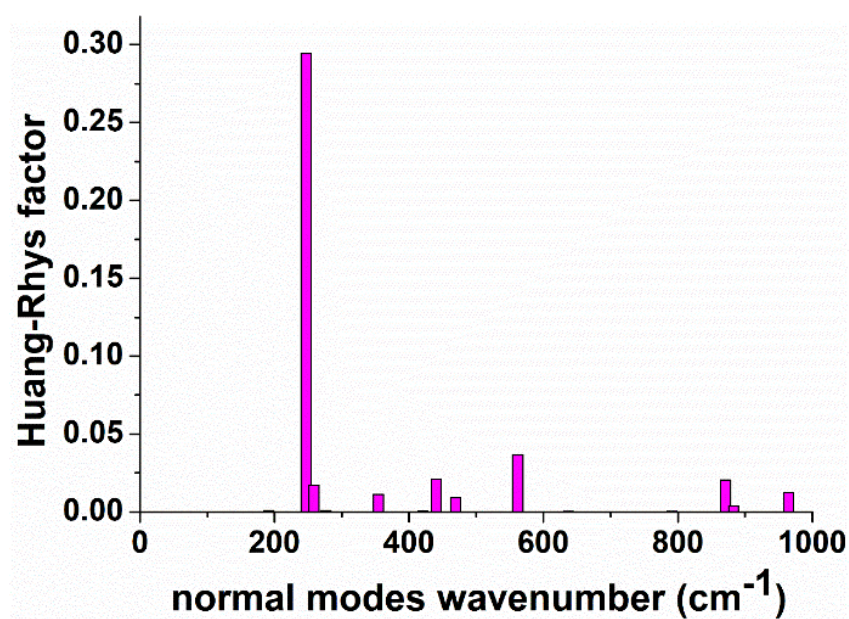Figure S10. Calculated Huang-Rhys factors versus the normal mode wavenumber for **10**.

Figure S11. Calculated Huang-Rhys factors versus the normal mode wavenumber for **11**.
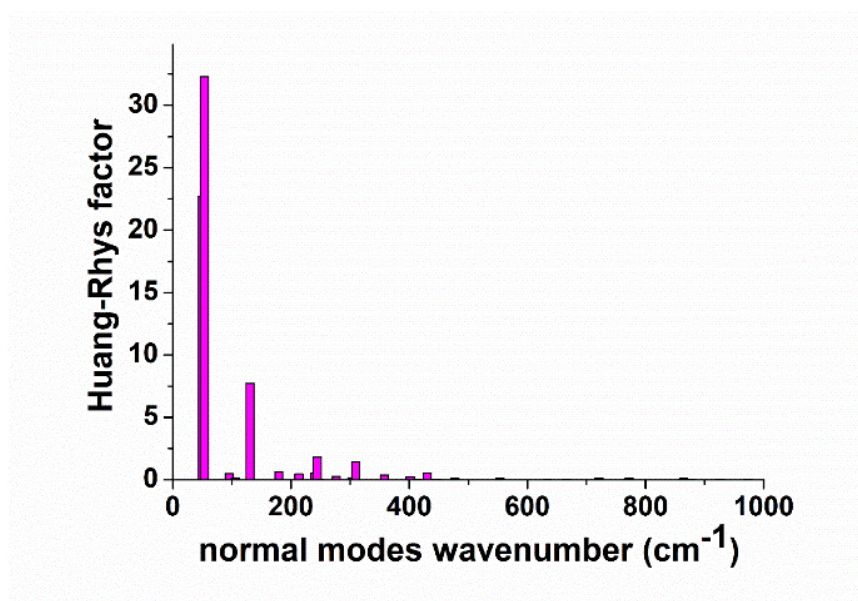


Figure S12. Calculated Huang-Rhys factors versus the normal mode wavenumber for **12**.
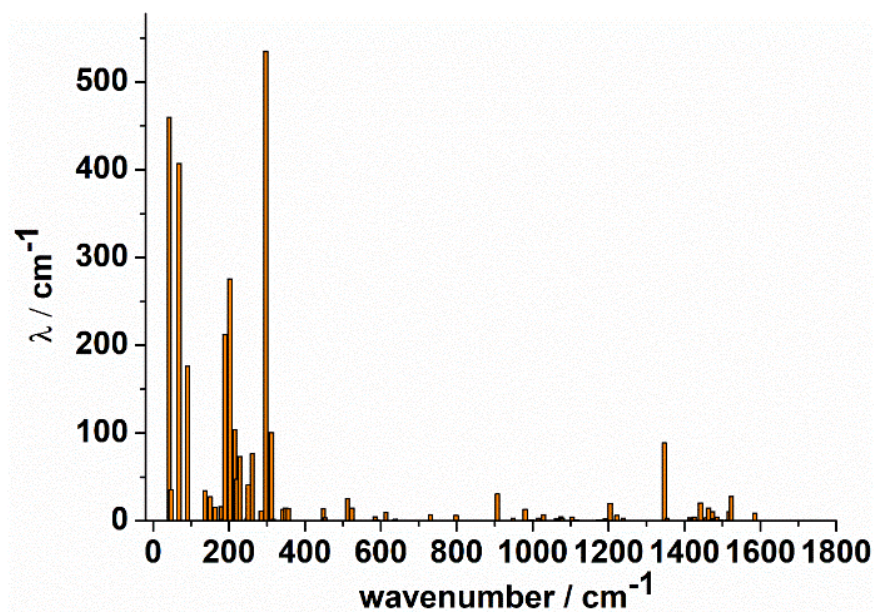
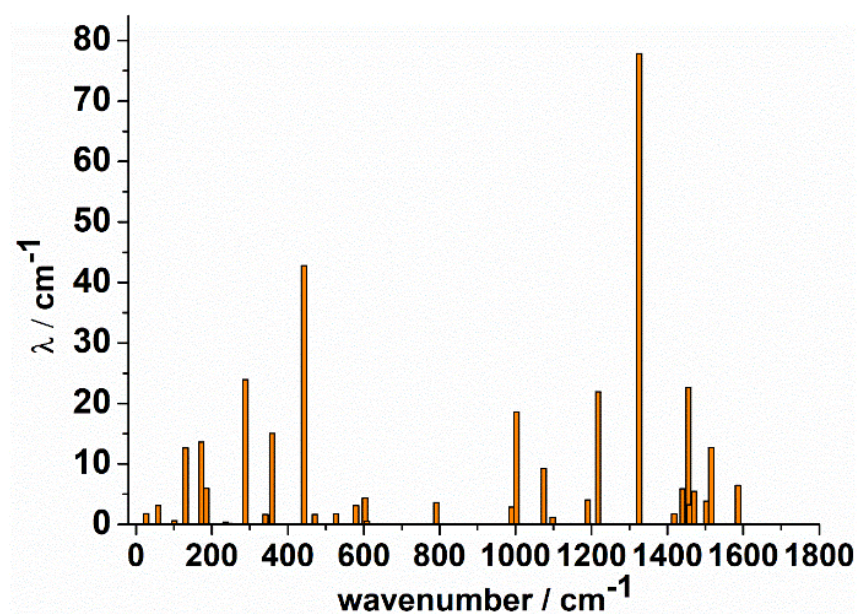Figure S13. Calculated reorganization energies versus the normal mode wavenumber for **3**.



Figure S14. Calculated reorganization energies versus the normal mode wavenumber for **4**.
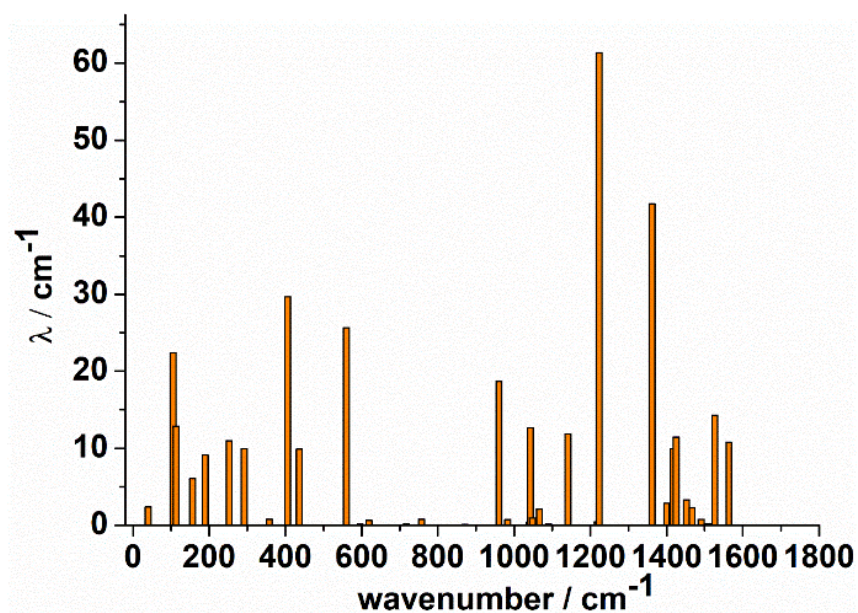
Figure S15. Calculated reorganization energies versus the normal mode wavenumber for **5**.
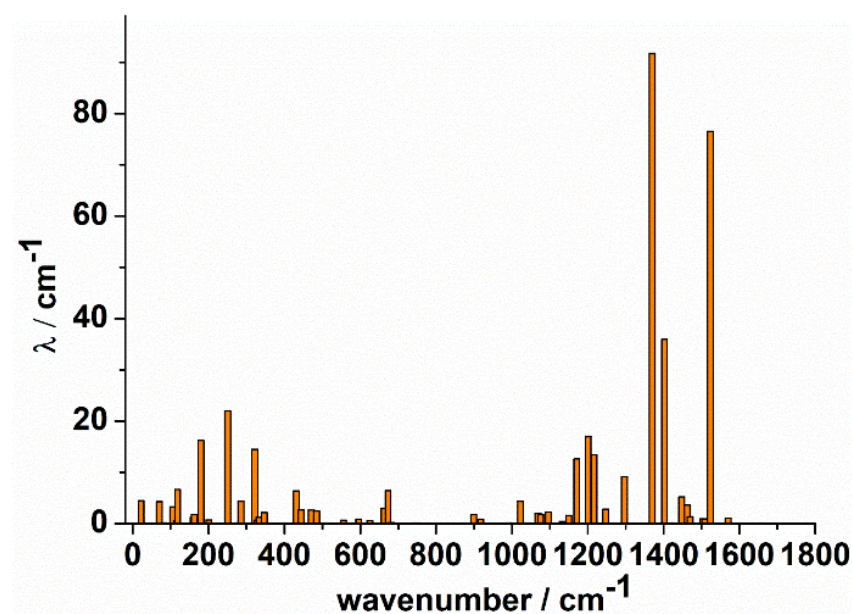


Figure S16. Calculated reorganization energies versus the normal mode wavenumber for **6**.

Figure S17. Calculated reorganization energies versus the normal mode wavenumber for **7**.



Figure S18. Calculated reorganization energies versus the normal mode wavenumber for **8**.

Figure S19. Calculated reorganization energies versus the normal mode wavenumber for **9**.



Figure S20. Calculated reorganization energies versus the normal mode wavenumber for **10**.
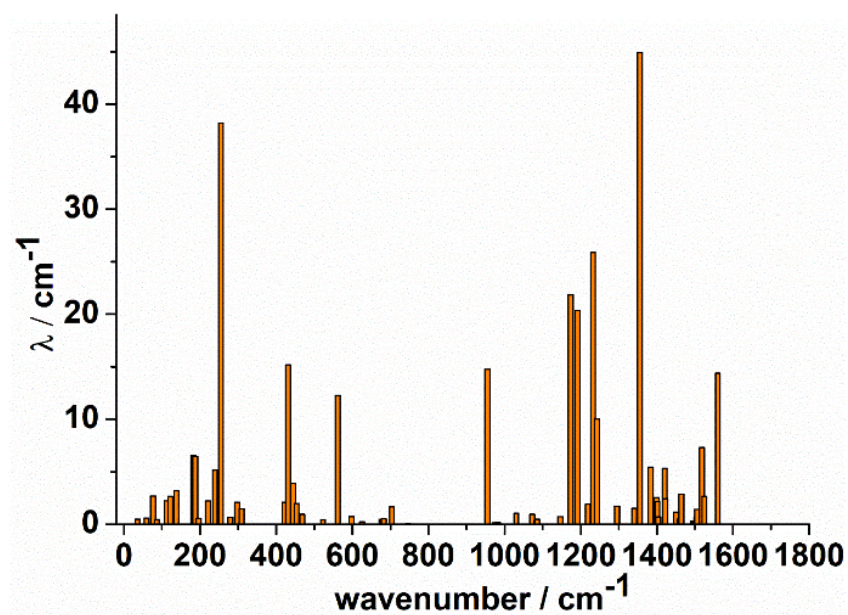
Figure S21. Calculated reorganization energies versus the normal mode wavenumber for **11**.
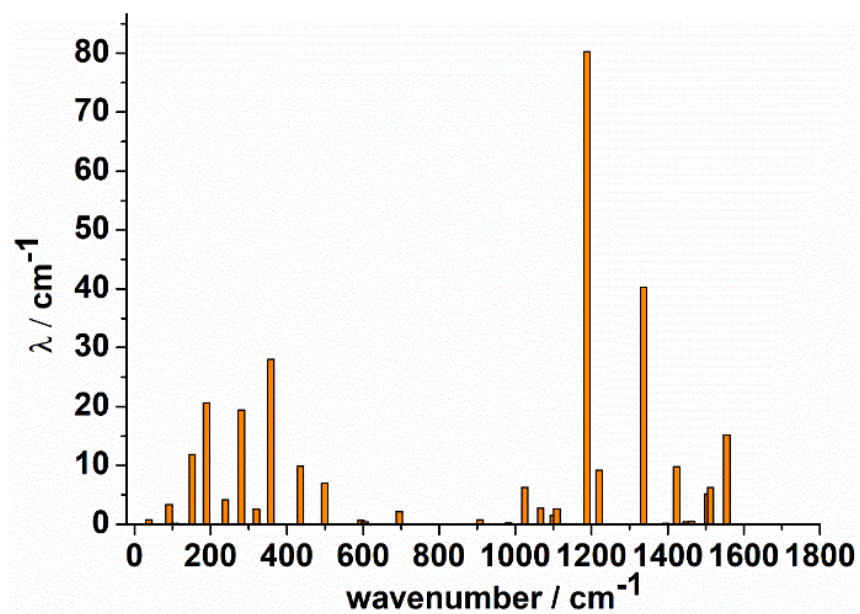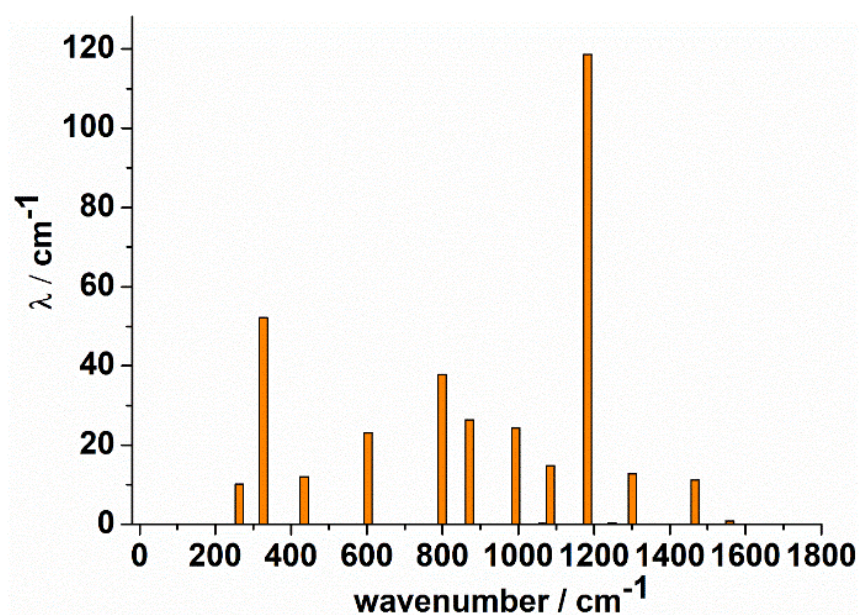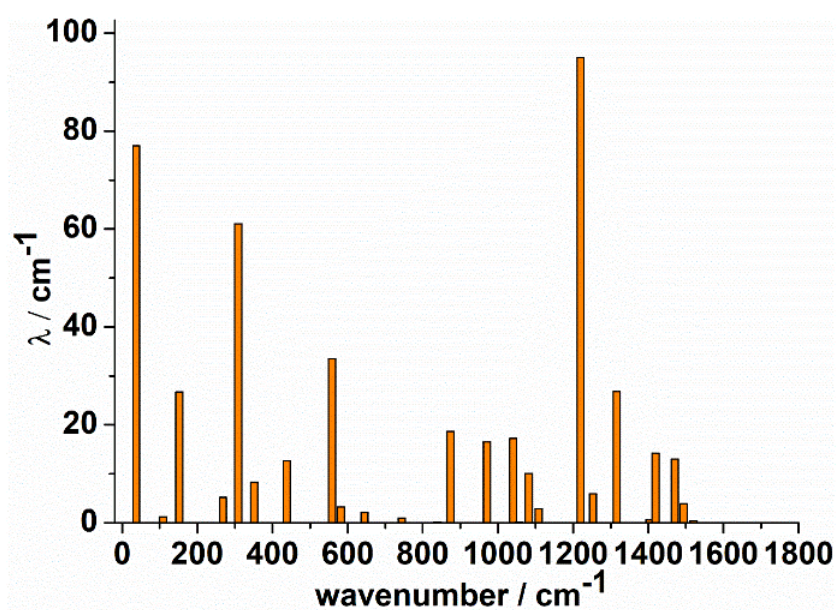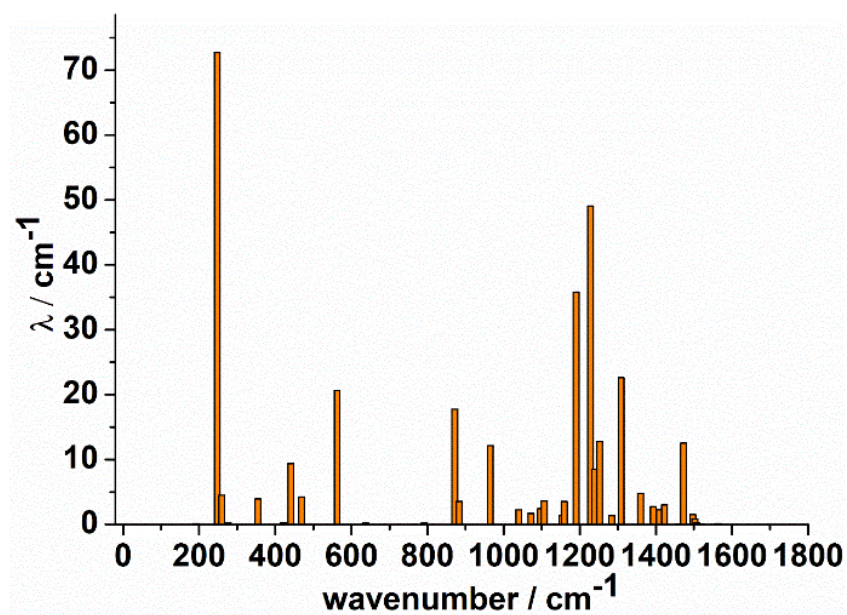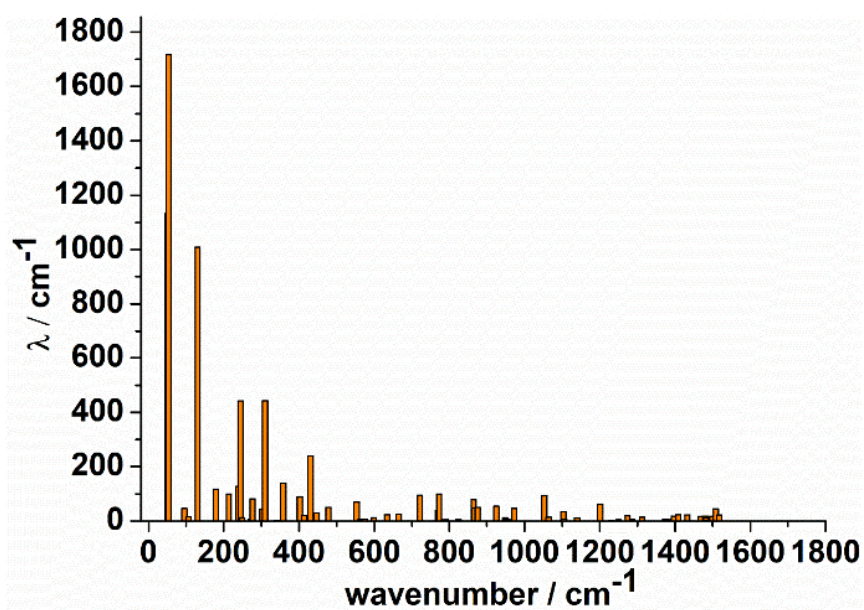


Figure S22. Calculated reorganization energies versus the normal mode wavenumber for **12**.

# Experimental Methods and Results

## Materials and general methods

Unless stated otherwise, all solvents and chemicals were purchased from commercial suppliers in analytical grade and used without further purification. The $^1$H and $^{13}$C NMR spectra were recorded on a Bruker AM 400 spectrometer, using TMS as an internal standard. High-resolution mass spectrometry data were obtained with a Waters LCT Premier XE spectrometer. UV-vis absorption spectra were collected on a Varian Cary 500 spectrophotometer, and fluorescence spectra measurements were performed on a Varian Cary Eclipse fluorescence spectrophotometer. Confocal fluorescence images were taken on a confocal laser scanning microscope (CLSM, Leica confocal microscope TCS SPS CFSMP).
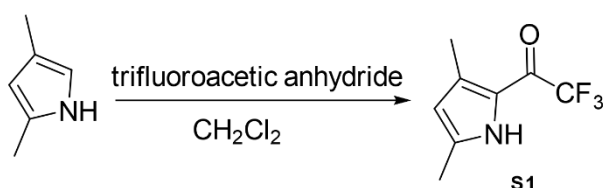
## Synthesis of CF₃-BODIPY (2)



Figure S23. Synthetic route of **S1**.

2,4-dimethylpyrrole (3 mL, 29.13 mmol) and trifluoroacetic anhydride (4.5 mL, 48.06 mmol) were dissolved in dry dichloromethane (30 mL) at 0 °C. Then the mixture was warmed to room temperature and stirred for 3 hours under an argon atmosphere. The reaction was quenched with saturated aqueous NaHCO$_3$ and extracted with CH$_2$Cl$_2$. The solvent was removed under reduced pressure, and then the crude product was purified by silica gel chromatography using petroleum ether/dichloromethane (v/v, 50:1) as the eluent to afford compound **1** as a white solid (4.6 g): Yield 83%. $^1$H NMR (400 MHz, CDCl$_3$, ppm) $\delta$: 5.98 (d, $J$ = 1.6 Hz, 1H, pyrrole-H), 2.37 (s, 3H, -C$\boldsymbol{H}_3$), 2.32 (s, 3H, -C$\boldsymbol{H}_3$).
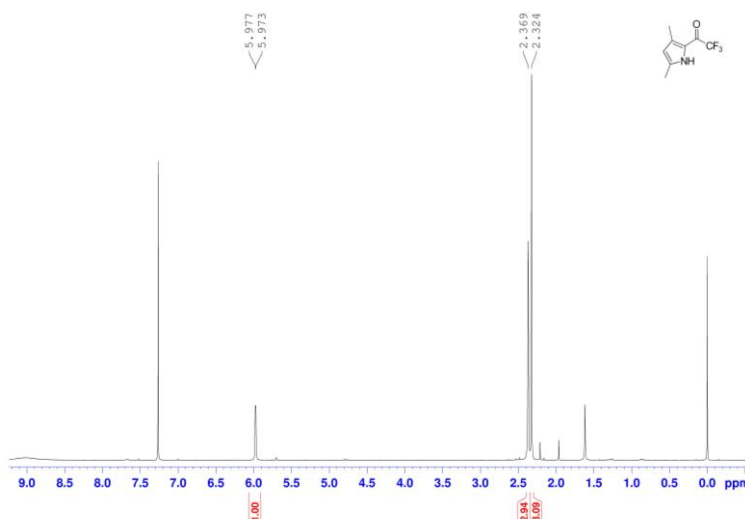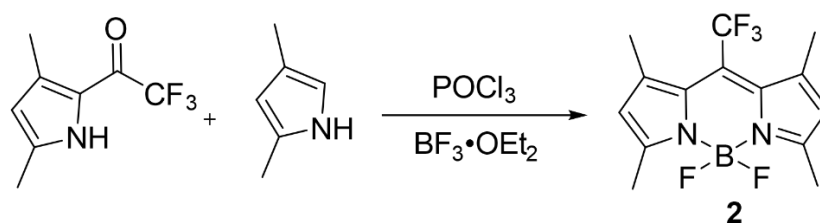


Figure S24. $^1$H NMR spectrum of **S1** in CDCl$_3$.

Figure S25. Synthetic route of **2**.

Compound **S1** (500 mg, 2.69 mmol) and 2,4-dimethylpyrrole (416 μL, 4.04 mmol) were dissolved in dry dichloromethane (20 mL). POCl$_3$ (336 μL, 2.47 mmol) was added to the mixture under argon atmosphere and stirred for 4 hours at room temperature. BF$_3$·OEt$_2$ (1 mL, 7.89 mmol) and triethylamine (1 mL, 7.17 mmol) were added to the reaction solution. After stirring for 10 min, the reaction mixture was extracted with CH$_2$Cl$_2$. The solvent was removed under reduced pressure, and then the crude product was purified by silica gel chromatography using petroleum ether/dichloromethane (v/v, 9:1) as the eluent to afford **2** as a golden yellow solid (442 mg): Yield 52%. $^1$H NMR (400 MHz, CDCl$_3$, ppm) $\delta$: 6.16 (s, 2H, pyrrole-H), 2.54 (s, 6H, -C$H_3$), 2.31 (s, 6H, -C$H_3$).
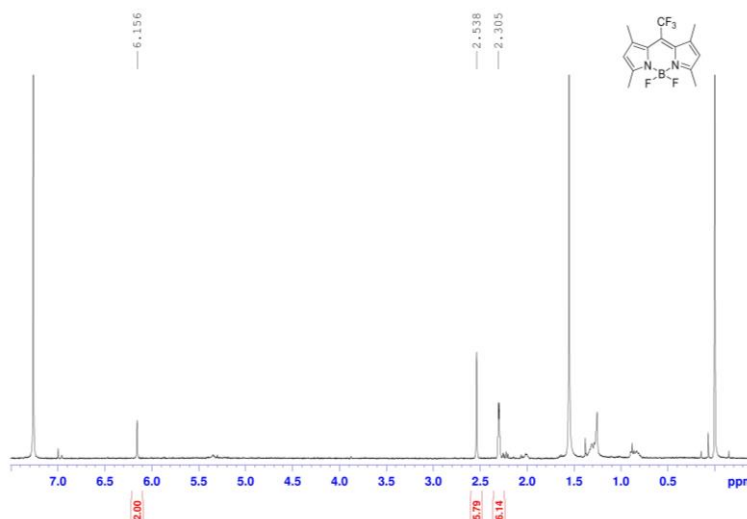


Figure S26. $^1$H NMR spectrum of **2** in CDCl$_3$.

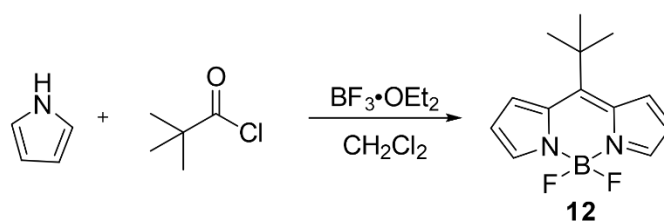Synthesis of **tBu-BODIPY (12)**



Figure S27. Synthetic route of **12**.

Pyrrole (1 g, 14.9 mmol) and pivaloyl chloride (894 mg, 7.45 mmol) were dissolved in dry dichloromethane (20 mL). Then the mixture was stirred for 12 h under an argon atmosphere. BF$_3$·OEt$_2$ (8 mL, 63.12 mmol) and triethylamine (3 mL,

21.51 mmol) were added to the reaction solution. After stirring for 2 h, the reaction mixture was extracted with $CH_2Cl_2$. The solvent was removed under reduced pressure, and then the crude product was purified by silica gel chromatography using petroleum ether/dichloromethane (v/v, 9:1) as the eluent to afford **12** as a red solid (332 mg): Yield 18%. ^{1}H NMR (400 MHz, $CDCl_3$, ppm) $\delta$: 7.82 (s, 2H, pyrrole-H), 7.67 (s, 2H, pyrrole-H), 6.54 (s, 2H, pyrrole-H), 1.73 (s, 9H, -C(C$H_3$)$_3$).
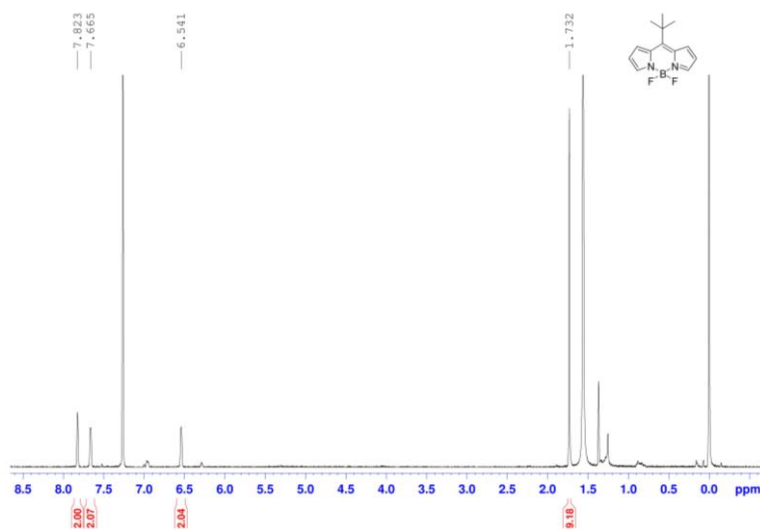


Figure S28. ^{1}H NMR spectrum of **12** in $CDCl_3$.

## Synthesis of **tBu-Flu** (**13**)
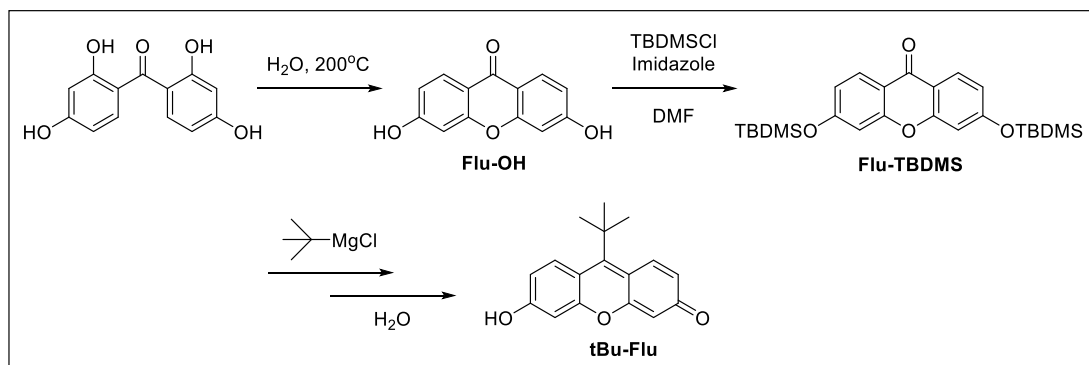


Figure S29. Synthetic route of **tBu-Flu** (**13**)

## Synthesis of **Flu-OH**

Bis(2,4-dihydroxyphenyl)methanone (5.0 g, 20.0 mmol), and ultrapure water (20 mL) were added in a hydrothermal synthesis reactor. Then the mixture was heated to 200 °C for 4 h. After cooling to room temperature, the mixture was filtered and the residue was washed with water (3 × 10 mL) to afford **Flu-OH** (3.3 g): Yield 72.4%. ^{1}H NMR (DMSO-$d_6$, 400 MHz, ppm) $\delta$: 8.00 (d, $J = 8.4$ Hz, 2H, phenyl-H), 7.87 (q, $J = 8.4$ Hz, 2H, phenyl-H), 6.83 (d, $J = 2.0$ Hz, 2H, phenyl-H).

Synthesis of **Flu-TBDMS**

**Flu-OH** (0.5 g, 2.2 mmol), TBDMSCl (2.0 g, 13.2 mmol), and imidazole (1.5 g, 22.0 mmol) were dissolved in DMF (45 mL) and kept stirring at room temperature for 2 h. The solvent was removed under reduced pressure, and then the crude product was purified by silica gel chromatography using dichloromethane as the eluent to afford **Flu-TBDMS** as a white solid (0.6 g): Yield 60%. $^1$H NMR (CDCl$_3$, 400 MHz, ppm) $\delta$: 8.20 (d, $J$ = 8.4 Hz, 2H, phenyl-H), 8.85 (s and d, 4H, phenyl-H), 1.01 (s, 18H, -C(C$H_3$)$_3$), 0.29 (s, 12H, -Si(C$H_3$)$_2$C(CH$_3$)$_3$).

Synthesis of **tBu-Flu (13)**

**Flu-TBDMS** (200 mg, 0.44 mmol) and *tert*-butylmagnesium chloride (4.50 mL, 2.20 mmol) were dissolved in dry THF (5 mL) under an argon atmosphere at room temperature. The resulting solution was kept stirring at room temperature for 2 h. Water (10 mL) was added to the mixture. Then the solvent was removed under reduced pressure, and then the crude product was purified by silica gel chromatography using dichloromethane as the eluent to afford **tBu-Flu** (62 mg): Yield 52%. $^1$H NMR (CDCl$_3$, 400 MHz, ppm) $\delta$: 7.49 (d, $J$ = 8.4 Hz, 2H, phenyl-H), 6.65 (q, $J$ = 8.4 Hz, 2H, phenyl-H), 6.60 (q, $J$ = 2.4 Hz, 2H, phenyl-H), 0.80 (s, 9H, -C(C$H_3$)$_3$).
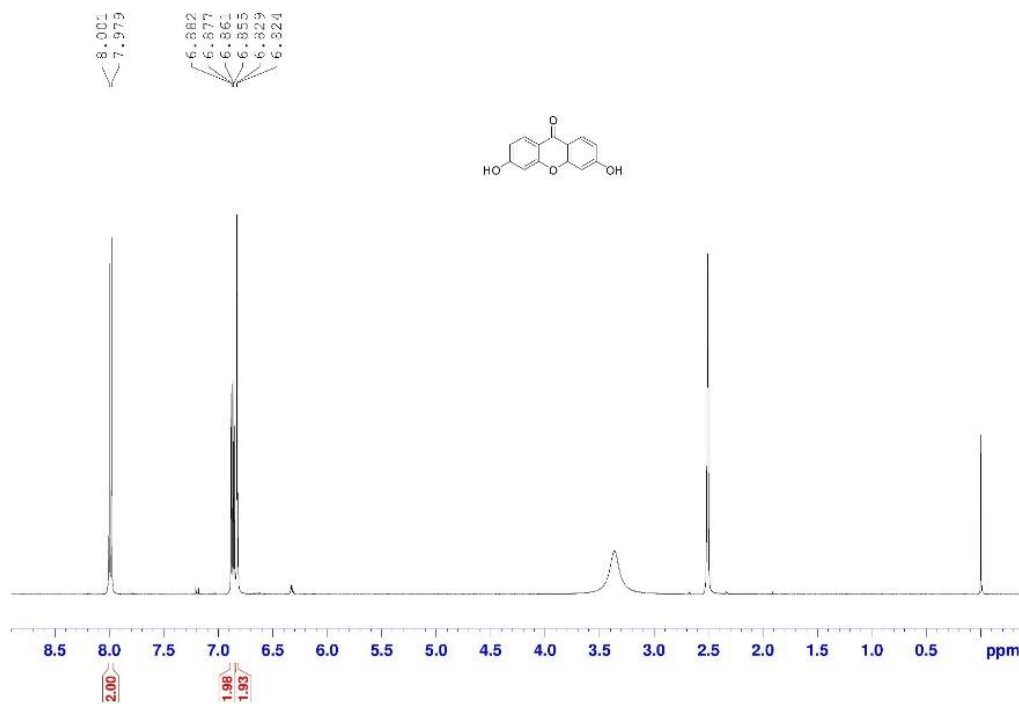


Figure S30. $^1$H NMR spectrum of Flu-OH in DMSO-$d_6$.
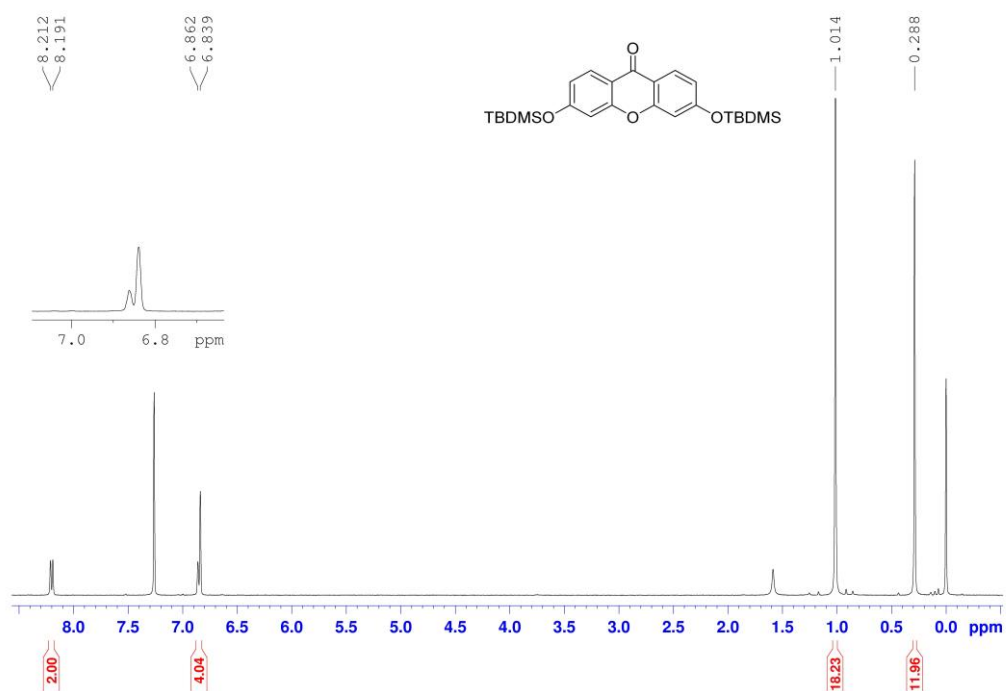
Figure S31. $^1$H NMR spectrum of Flu-TBDMS in CDCl$_3$.
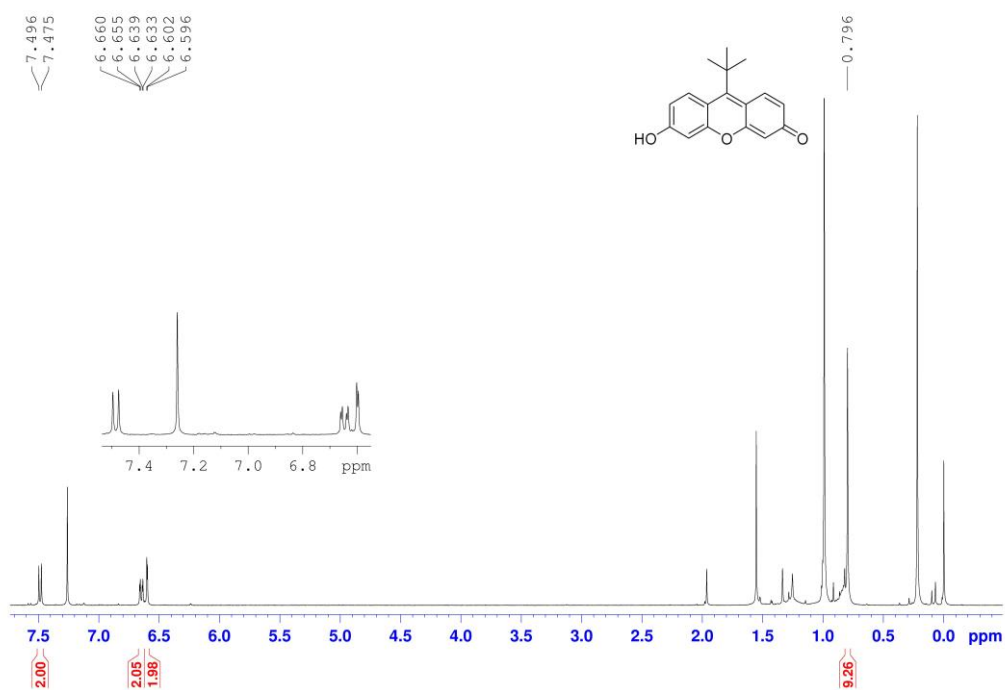


Figure S32. $^1$H NMR spectrum of tBu-Flu (**13**) in CDCl$_3$.
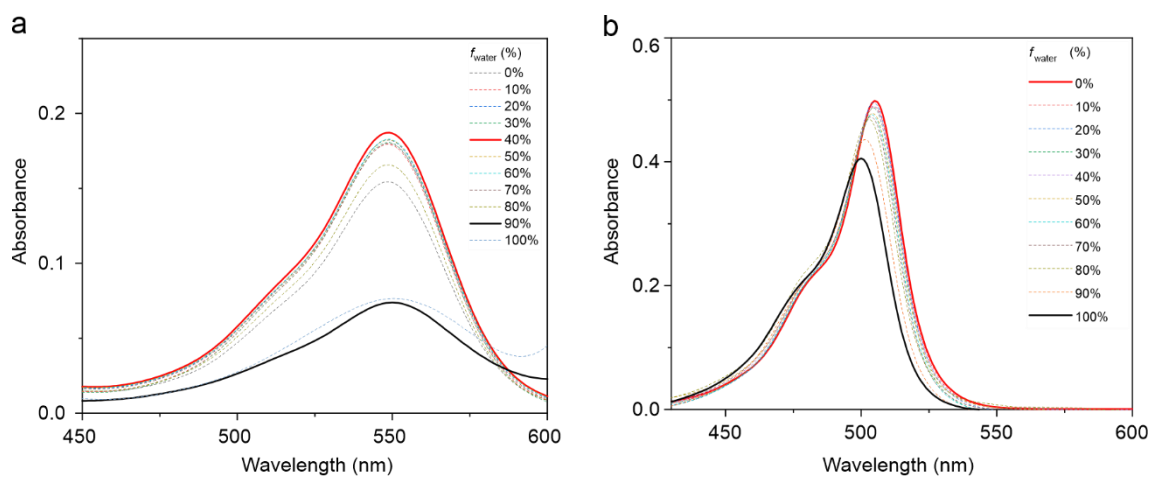
Figure S33. The UV-vis absorption spectra of **2** (a) and **12** (b) in acetonitrile/water and THF/water mixtures, respectively.
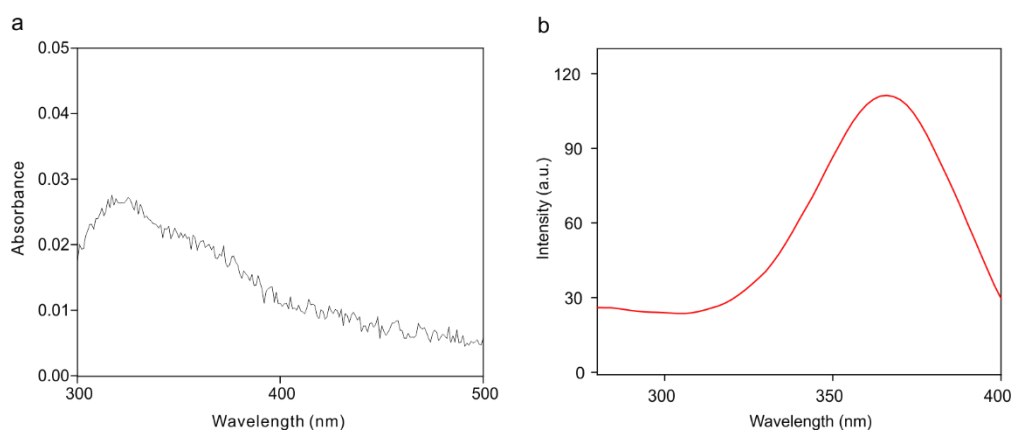


Figure S34. UV-Vis absorption (a) and fluorescence excitation spectra (b) of **13** in the binary mixture of DMSO and water (v:v = 50:50). The UV-vis absorption and excitation peaks are located at 325 and 375 nm, respectively. The difference is mainly derived from multitudinous aggregation forms. [**13**] = 10 μM.

# Possible Reasons for the Decrease of Fluorescence Intensities at High Water Concentrations

When the water content exceeds 80% in the binary mixture of THF/CH$_3$CN/DMSO and water, a decrease in the emission intensities of our AIEgens was observed. This phenomenon is not limited to our AIEgens but has also been reported in several other AIEgen systems.

Determining the exact underlying reasons for this drop in fluorescence intensities can be challenging as it may involve multiple factors. However, we suspect that the following factors may contribute to this phenomenon:

**The primary "local" inner filter effect**

In highly concentrated solutions, the excitation beam can be attenuated by the sample, resulting in strong fluorescence only from the surface facing the excitation beam. As a consequence of the excitation beam attenuation, the centre of the cuvette, which is observed by the emission monochromator in the fluorescence spectrometer, may exhibit lower or even no fluorescence emission, thereby affecting the detected signal. This phenomenon is referred to as the primary inner filter effect. To mitigate the primary inner filter effect, fluorescence measurements are typically conducted using low sample concentrations to minimize the attenuation of the excitation beam.

As the water content increases, promoting molecular aggregation, the sizes of the molecular aggregates may start to grow. Consequently, the "local" concentration within these aggregates becomes very high, and only the molecules near the surface of the aggregates are efficiently excited and emit fluorescence. In this scenario, the excitation beam is attenuated within the inner core of the aggregates, leading to weak or no fluorescence in this region (Figure S36).
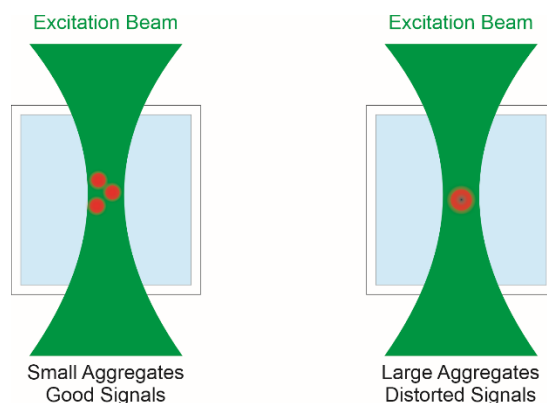


Figure S35. Schematic illustration depicting the occurrence of the "local" primary inner filter effect as the sizes of the aggregates increase.

**The secondary "local" inner filter effect**

Furthermore, in cases where the excitation and emission spectra significantly overlap, the light emitted in the centre of the aggregate can be reabsorbed by the aggregate itself. We refer to this phenomenon as the secondary "local" inner filter effect.

**The scattering of the excitation beam**

As the size of the molecular aggregates continues to grow with increasing water content, reaching dimensions comparable to the wavelength of the excitation beam, strong scattering is expected to occur. This scattering phenomenon can result in a decrease in fluorescence intensity.

**Precipitation of large molecular aggregates**

As the water content further increases, the limited solubility of the dyes may lead to the precipitation of the molecules. This precipitation can result in a reduction of the emission intensity recorded by the fluorescence spectrometer, as the signals collected are primarily from the centre of the cuvettes where the precipitated dyes are not present.
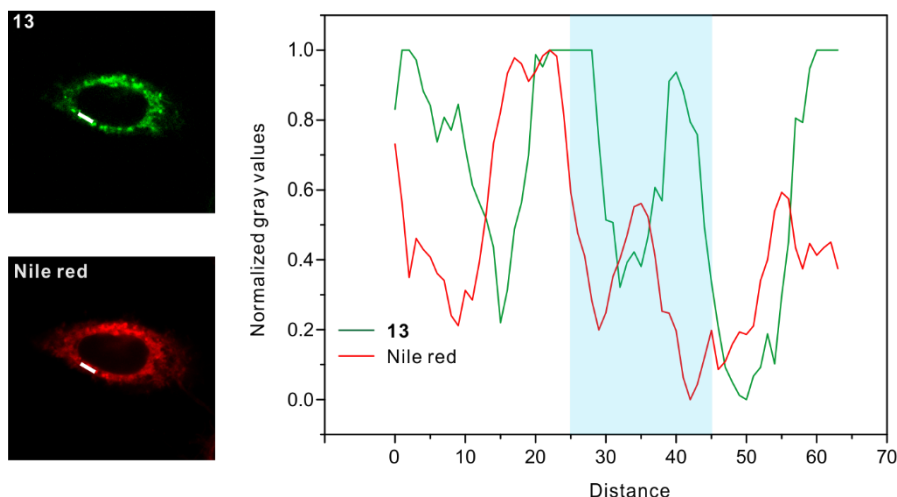
Figure S36. Intensity profiles of the red linear region of interest in merged images.

# References

1.  M. J. Frisch, G. W. Trucks, H. B. Schlegel, G. E. Scuseria, M. A. Robb, J. R. Cheeseman, G. Scalmani, V. Barone, G. A. Petersson, H. Nakatsuji, X. Li, M. Caricato, A. V. Marenich, J. Bloino, B. G. Janesko, R. Gomperts, B. Mennucci, H. P. Hratchian, J. V. Ortiz, A. F. Izmaylov, J. L. Sonnenberg, Williams, F. Ding, F. Lipparini, F. Egidi, J. Goings, B. Peng, A. Petrone, T. Henderson, D. Ranasinghe, V. G. Zakrzewski, J. Gao, N. Rega, G. Zheng, W. Liang, M. Hada, M. Ehara, K. Toyota, R. Fukuda, J. Hasegawa, M. Ishida, T. Nakajima, Y. Honda, O. Kitao, H. Nakai, T. Vreven, K. Throssell, J. A. Montgomery Jr., J. E. Peralta, F. Ogliaro, M. J. Bearpark, J. J. Heyd, E. N. Brothers, K. N. Kudin, V. N. Staroverov, T. A. Keith, R. Kobayashi, J. Normand, K. Raghavachari, A. P. Rendell, J. C. Burant, S. S. Iyengar, J. Tomasi, M. Cossi, J. M. Millam, M. Klene, C. Adamo, R. Cammi, J. W. Ochterski, R. L. Martin, K. Morokuma, O. Farkas, J. B. Foresman and D. J. Fox, Gaussian 16 Rev. C.01, Wallingford, CT, 2016.
2.  Y. Zhao and D. G. Truhlar, The M06 suite of density functionals for main group thermochemistry, thermochemical kinetics, noncovalent interactions, excited states, and transition elements: two new functionals and systematic testing of four M06-class functionals and 12 other functionals, *Theor. Chem. Acc.*, 2008, **120**, 215-241.
3.  F. Weigend and R. Ahlrichs, Balanced basis sets of split valence, triple zeta valence and quadruple zeta valence quality for H to Rn: Design and assessment of accuracy, *PCCP*, 2005, **7**, 3297-3305.
4.  A. V. Marenich, C. J. Cramer and D. G. Truhlar, Universal Solvation Model Based on Solute Electron Density and on a Continuum Model of the Solvent Defined by the Bulk Dielectric Constant and Atomic Surface Tensions, *J. Phys. Chem. B*, 2009, **113**, 6378-6396.
5.  T. Lu and F. Chen, Multiwfn: A multifunctional wavefunction analyzer, *J. Comput. Chem.*, 2012, **33**, 580-592.
6.  G. M. Morris, R. Huey, W. Lindstrom, M. F. Sanner, R. K. Belew, D. S. Goodsell and A. J. Olson, AutoDock4 and AutoDockTools4: Automated docking with selective receptor flexibility, *J. Comput. Chem.*, 2009, **30**, 2785-2791.
7.  W. L. J. C. N. o. p. c. DeLano, Pymol: An open-source molecular graphics tool, *Protein Crystallogr.* 2002, **40**, 82-92.
8.  Y. Niu, W. Li, Q. Peng, H. Geng, Y. Yi, L. Wang, G. Nan, D. Wang and Z. Shuai, MOlecular MAterials Property Prediction Package (MOMAP) 1.0: a software package for predicting the luminescent properties and mobility of organic functional materials, *Mol. Phys.*, 2018, **116**, 1078-1090.
9.  S. Choi, J. Bouffard and Y. Kim, Aggregation-induced emission enhancement of a meso-trifluoromethyl BODIPY via J-aggregation, *Chem. Sci.*, 2014, **5**, 751-755.